Performance of the double-Wien filter of the Neoma MC-ICPMS/MS with an application to copper stable isotope compositions

Philippe Télouk, Emmanuelle Albalat, Bernard Bourdon, Francis Albarède, Vincent Balter

Performance of the double-Wien filter of the Neoma MC-ICPMS/MS with an application to copper stable isotope compositions

Philippe Télouk [1], Emmanuelle Albalat [1], Bernard Bourdon [1], Francis Albarède [1], Vincent Balter [1,*]

1 : LGL-TPE, UMR 5276, CNRS, Ecole Normale Supérieure de Lyon, Université de Lyon 1

* corresponding author: Vincent.Balter@ens-lyon.fr

ABSTRACT

The new Neoma MC-ICPMS/MS is equipped with a prefiltering system consisting of a double-Wien filter and a collision/reaction cell whose performances are challenged using different combinations of magnetic and electrostatic field values and adjustable slit apertures. The results show an asymmetrical attenuation of transmission relative to the chosen axial mass-to-charge value, with higher efficiency at removing low masses than high masses, even when magnetic induction is minimal. The resulting asymmetry of the bandpass window is fully predictable by theoretical calculations of ion trajectories in a Wien filter, either as a function of the magnetic field value or that of the aperture of the adjustable slit. With an axial mass-to-charge value set at ^{120}Sn, the vertical deviation for a magnetic field value at 100% will be approximately 3 mm and 4 mm for a variation of mass-to-charge of ± 20%, respectively. In these conditions, Ar was already barely detectable with the lowest magnetic field value (10%) and a fully open adjustable slit, while Pb is quantitatively transmitted. We then use the prefiltering system to remove on-line the $^{40}Ar^{23}Na^{+}$ compound that produces an isobaric interference with ^{63}Cu, hampering high-precision measurement of Cu stable isotope composition ($^{65}Cu/^{63}Cu$). While Na is not transmitted thanks to the double-Wien filter, $^{40}Ar^{23}Na^{+}$ still interferes with ^{63}Cu, demonstrating that this argide is produced in the plasma source but not in the reaction cell. Helium in the collision/reaction cell is necessary to remove the $^{40}Ar^{23}Na^{+}$ interference. The MS/MS technology of the Neoma allows for the correction of the $^{40}Ar^{23}Na^{+}$ interference up to a Na/Cu ratio of 10, where other classic MC-ICPMS already show an offset of the Cu stable isotope composition for a Na/Cu ratio of 1. The inability to correct the Cu stable isotope composition with a Na/Cu ratio higher than 10 suggests that the Na-based interference is no longer spectral and becomes linked to the matrix. We next measure the Cu stable isotope composition in eight certified reference materials prepared with a simple automated single step ion-chromatography procedure to purify Cu. The results show a very good agreement with previously reported values. The overall results suggest that the MS/MS technology of the Neoma MC-ICPMS allows efficient on-line isolation of analytes, therefore reducing potential spectral and matrix interferences to permit much better resolved and controlled subsequent effects in the collision/reaction cell.

INTRODUCTION

Copper has only two stable isotopes (^{63}Cu and ^{65}Cu), whose relative abundances (^{63}Cu = 69.17% and ^{65}Cu = 30.83%) have been determined in the 1960's by thermal ionization mass spectrometry (TIMS) [1]. Isotopic variations were associated with poor analytical uncertainty (2 ‰/amu [1]) because ionization yields of Cu were too low with the TIMS technique. It was not until the late 1990's with the arrival of the first commercialized multi-collector inductively coupled plasma mass spectrometry (MC-ICPMS), at the time the Plasma 54 (VG Elemental, now ThermoFisher Scientific, Bremen), that it was possible to achieve precise (0.02 ‰/amu) Cu isotope ratio measurements [2]. The pioneering work of Maréchal et al. [2] showed that the instrumental mass bias of MC-ICPMS can be corrected by a combination of standard/sample bracketing and elemental doping with Zn, which was further modified by using Ni [3,4] or Ga [5,6]. The overall consistency of the measurements of Cu isotope compositions by MC-ICPMS leads to the rapid development of applications in various fields such as cosmochemistry [7,8], igneous [9,10], ore [11,12], sediment [13,14] and river [15,16] geochemistry, oceanography [17,18], tracing atmospheric [19–21] and soil [22–24] pollution, assessing the diagnosis and prognosis of metabolic [25–27] and neurodegenerative [28–30] diseases, cancer [31–33], but also in palaeoanthropology [34–36] and archaeology [37–39].

Prior to isotopic analysis, Cu needs to be separated from the matrix and further purified using ion-exchange chromatography. Many protocols exist [3,40–42], generally based on the use of the strongly basic AG MP-1 anion exchange resin (100–200 mesh, chloride form). These protocols are usually effective for the purification of Cu, but extreme care must be taken for the removal of Na, because an argide $^{40}Ar^{23}Na^{+}$ compound interferes with the ^{63}Cu isobar. Removing Na can be done quite easily for silicate materials, which generally exhibit a Na/Cu ratio ranging from 10^2 to 10^3, but can be extremely challenging for biological fluids (urine, Na/Cu ~ 8.10^4; plasma, Na/Cu ~ 3.10^6) and above all, seawater, Na/Cu ~ 5.10^7). For the extreme case of seawater, large volumes of eluent for Na separation and Cu purification are necessary for the handling of which automatic procedures have been recently developed [40,42]. Contrasting with these off-line procedures, an alternative on-line procedure now exists thanks to the MS/MS technology of the Neoma MC-ICPMS. The MS/MS technology consists of a precell mass filter and a collision cell[43]. Initially, the precell mass filter was a bespoke quadrupole, which allowed a prototype Proteus to measure several isotope systems [44–46]. Lack of sensitivity and non-reproducible mass bias prevented the Proteus from being widely adopted by the MC-ICPMS

community, and the low-energy quadrupole was replaced by a high-energy double Wien filter on the Vienna prototype [47,48].

The double-focusing electrostatic analyzer and magnetic sector geometry is standard and inspired from that of the Neptune MC-ICPMS, while the collection system has been totally redesigned as described in Dauphas et al. [49] and Télouk et al. [50].

In this study, we first explore the performance of the double-Wien filter to on-line prefilter ions with different m/z using various combinations of B and S values. Second, we compare the performances of the Neoma MC-ICPMS/MS to those of standard MC-ICPMS and third, we measure the $^{65}Cu/^{63}Cu$ ratio in certified reference materials that have experienced a single purification step to validate the overall procedure.

EXPERIMENTAL

Reagents and materials

All experiments were carried out in laminar flow hoods in a clean laboratory at the LGL-TPE (Ecole Normale Supérieure de Lyon). Acids (HNO_3, HCl, and HF) were double distilled to reduce blank contaminations. Ultrapure water (resistivity > 18.2 MΩ.cm) was obtained from a Milli-Q Element water purification system (Merck Millipore, Bedford, MA, USA). The performances of the double-Wien prefiltering was assessed using the multi-element standard solution SCP33MS containing 33 elements (SCP Sciences, Québec, Canada) diluted to 200 ng/mL. Synthetic solutions were prepared by diluting Na and Zn Specpure solutions (Alfa Aesar, Karlsruhe, Germany) and Cu SRM-976 solution (National Institute of Standards and Technology, Gaithersburg, MD, USA) to reach a final concentration of 200 ng/mL for Cu and Zn and various Na/Cu ratios. Eight geological certified reference materials (CRM) were obtained from the United States Geological Survey (USGS) and include the BHVO-1 Hawaiian basalt [51], Glass Mountain rhyolite RGM-1 [51], the Columbia River basalt BCR-1 [52], the AGV-2 Guano Valley andesite [52], the BIR-1 Icelandic basalt [53], the DNC-1 North Carolina dolerite [53], the Centreville diabase W2a [53], and the Japanese alkali basalt JB1-a [54] from the Geological Survey of Japan (GSJ). A minimum sample size of 100 mg was weighed for CRM to avoid measurement uncertainties due to the heterogeneity of the reference material powder. Certified reference materials were digested with a mixture of 5 mL of 27 M distilled HF and 2.5 mL of 15 M distilled HNO_3 at 120°C for 12 hours and evaporated to dryness. Fluorides were redissolved using 2 mL of 6M HCl and heated on a hotplate at 100°C for 12 hours and

then evaporated to dryness. The chemical separation of Cu was achieved using the automated chromatography system prepFAST-MC (Elemental Scientific, Omaha, USA) loaded with 500 µL of CU resin (Triskem, Rennes, France) following the procedure of Enge et al. [55].

Instrumentation

The MS/MS equipment consists of a double-Wien filter and a collision/reaction cell [47]. The Wien filter is an important device in charged particle optics because it is a static field mass filter that deflects charged particles according to their velocity [56], or equivalently their mass-to-charge ratio (m/z). While the Wien filter properties can also be used in electron microscopy [57], we will consider here the case where charged particles are ions. The Wien filter consists of a uniform electrostatic ($\vec{E}$) field orthogonal to a magnetic ($\vec{B}$) field. Charged particles passing through this arrangement of fields are subject to an electrostatic force ($\vec{F}_E = q\vec{E}$) and a magnetic force ($\vec{F}_B = q\ \vec{v} \times \vec{B}$), where q and $\vec{v}$ are the charge and the velocity, respectively, of the ion. For a collimated ion beam perpendicular to both fields, the axial transmission of an ion m_0 with a velocity v_0 will happen when $v_0 = |\overrightarrow{E}| / |\overrightarrow{B}|$ (or $v_0 = E / B$). For ions with the same kinetic energy and $m < m_0$, $v > E / B$ because lighter ions travel faster, this ion beam will be deflected in the opposite direction of the $\vec{E}$ field (Figure 1). Inversely, for ions with $m > m_0$, the ion beam will be deflected in the direction of the $\vec{E}$ field because $v < E / B$ (Figure 1). The mass prefiltering system of the Neoma MC-ICPMS/MS is a double-Wien filter, with the first filter deflecting ions away from the axial trajectory and the second filter refocusing ions back towards the axial trajectory, in both cases according to their ion velocity. Both Wien filters are equipped with an array of upper and lower baffles to avoid reflection on the side walls of ions with a too great angle of deflection and to avoid charging of the electrodes [47]. After being vertically deflected apart from the axial trajectory, those ions with a too large m/z difference relative to m_0/z are not selected using an adjustable slit located between the two Wien filters. A combination of E, B, and adjustable slit aperture (S) values thus permits the transmission of a certain mass range through the inversion lens (Figure 1). The inversion lens is an Einzel lens that inverts the divergent trajectories of ion beams with m/z different from m_0/z towards the axial position, in inverse proportion to the degree of deviation introduced by the first Wien filter [46]. The inversion happens without altering energy, and the different ions enter the

second Wien filter as an uncollimated beam. The two Wien filters are of similar geometry, and their E and B fields are identical and controlled by a unique power supply. Thus, in the second Wien filter, ions with m < m_0 will be deflected in the opposite direction of the $\vec{E}$ field (and inversely for ion m < m_0), such that the ion beam becomes collimated again before the exit aperture. The mass prefilter contains four lenses that need to be tuned accordingly (Figure 1). The first lens (L1) focuses the ion beams through the adjustable slit, L2 (the inversion Einzel lens) bends the ion beams back toward the second Wien filter, the third lens (L3) focuses the ion beam into the exit aperture and the fourth lens (L4) focuses the ion beams to the collision/reaction cell (CRC), where they are kept focused using an hexapole despite scattering due to collisions with gas (Figure 1). The CRC allows the introduction of four different reactive (O_2, NH_3, H_2) and non-reactive (He) gases. The interfering species, which are polyatomic or molecular ions, collide with the cell gas more frequently than analyte ions because they have a larger collisional cross section. The mechanism for the elimination of the pre-existing polyatomic ions in collision with a non-reactive gas is the selective energy loss displayed by polyatomic ions compared with monoatomic ions. By applying a small, fixed bias voltage at the cell exit, it is possible to keep the polyatomic ions and newly formed species in the CRC while monoatomic ions have sufficient kinetic energy to exit. [58].

The Cu isotopic compositions were measured using the Nu Plasma MC-ICPMS (Nu Instruments, Wrexham, UK) following the original procedure described by Maréchal et al. [2], or using the Neoma MC-ICPMS/MS. The instrument parameters are summarized in Table 1. On the day of analysis, Cu-purified solutions were diluted in a Zn-doped solution (Zn JMC 3–0749L, Johnson Matthey Royston, UK) to match the concentration of the standard bracketing solution (200 ng/mL). Instrumental mass bias and temporal drift were corrected with an exponential law using Zn as an internal standard, combined with sample-standard bracketing, as recommended by Maréchal et al. [2]. All the results of isotopic measurements are given in the delta notation (expressed in ‰) and reported relative to the international isotopic standard solutions SRM-976 (National Institute of Standards and Technology, Gaithersburg, MD, USA) using:

$$\delta^{65}\mathrm{Cu} = \left[\frac{\left(^{65}\mathrm{Cu}/^{63}\mathrm{Cu}\right)_{sample}}{\left(^{65}\mathrm{Cu}/^{63}\mathrm{Cu}\right)_{standard}} - 1\right] \times 1000$$

We use the '33 Elements' solution at 200 ng/mL and mass scans ranging between 20 to 250 atomic mass units (amu) with an axial value set at the middle of the mass range, i.e., at ^{120}Sn and then at ^{63}Cu. Closing the slit necessitates to tune the E value by few volts. All statistical analyses was performed using the R software [59].

RESULTS AND DISCUSSION

Prefiltering performances

We first obtain a scan with the adjustable slit fully open (S = 100%) and minimal magnetic field (B = 10%, figure 2A) for a m_0 set at 120 amu (^{120}Sn). This configuration represents the basic instrumental conditions that the MS/MS will alter either with varying magnetic field, or closing the adjustable slit, or a combination thereof. It is noteworthy that these basic instrumental conditions already influence the transmission of low masses at about 100 amu away from m_0. Indeed, the minimal B value totally suppresses the signal intensities of elements such as Na, Mg, and S (figure 2A), and, of interest, also Ar, whose signal is only ~0.3 V for ^{40}Ar and ~1 V for ^{40}ArH. The prefiltering effects are asymmetrical, as high masses are transmitted efficiently (figure 2A). We next explore the effect of augmenting the magnetic field with an increment of ten percent of B, while keeping a constant E/B ratio and the adjustable slit fully open. Figure 2B shows the difference in signal intensities between two consecutive B increments of ten percent. The transmission of the elements in the range of 40 to 70 amu is completely eliminated when B is increased to 20%, and the transmission of the elements in the range of 70 to 90 amu is completely eliminated when B is increased to 30% (figure 2B). Lead is no longer transmitted for B = 40%. Slightly increasing B to 20% or 30% not only decreases the transmission of elements with low and high masses, but also increases that of elements with intermediate masses, i.e., close to m_0 = 120 amu (figure 2B). This can be explained by an enhanced transmission of elements with intermediate masses that is made easier by the removal of Ar^+ ions that produce significant space charge with a defocusing effect. Increasing the B value up to 40% reduces the signal intensities by about 80% for elements being ten amu lighter than the 120 m/z. However, when B is set ≥ 70%, the transmission likely becomes unstable as some masses slightly higher than the 120 m/z exhibit both increased and decreased voltages (figure 2B). A close-up from 90 to 150 m/z is given in Figure S1. Observed enhanced signal intensities can be significant (~ 2 V) but remain lower than generalized reduced signal intensities (~ -8 V). Measuring both enhanced and reduced

transmission for a given mass is obviously an artifact. A high measurement rate during scan acquisitions (about 20 measurements by amu) produces a lot of data, which can yield positive or negative differences when subtracted from two consecutive scans. Overall, this indicates that the instrument is suffering from unstable conditions at high B values. The performance of the MS/MS prefilter at high B values requires further investigation, but we anticipate that setting such high B values to remove elements will instead be preferentially achieved by closing the adjustable slit.

We next study the prefiltering effects for B values set at 10%, 30%, or 50%, E/B being constant, and with the adjustable slit fully open, or 50% or 70% closed (S = 100%, 50% and 30%, respectively). The resulting scans are given in Figure 3. Closing the adjustable slit when B is minimal produces very asymmetrical effects, with high masses not being affected until the slit is 50% closed, while low masses are filtered efficiently. The magnetic field must be set at half its maximum value, with a fully open adjustable slit to obtain a more symmetrical filtering. This combination (B = 50%, S = 100%) produces a shape of the bandpass window equivalent to that with B = 30% and S = 50%, for which masses are sharply filtered at about 40 amu away from the axial 120 m/z. Decreasing the width of the bandpass window to 30 amu from either side of the axial 120 m/z is obtained using combinations of B = 50% and S = 50%, or B = 30% and S = 30%. A half width of 20 amu of the bandpass window can be obtained with a combination of B = 50%, S = 30%. Thus, the behavior of the MS/MS prefilter is in agreement, but for low masses only, with the expectations of Craig et al [48] for the Vienna prototype, e.g., that closing the slit will decrease the overall size of the bandpass window without altering the sides steepness. However, further increasing B by 20 percent (to 50%) with a full open adjustable slit efficiently steepens the bandpass window on the low mass side but does not greatly affect high masses. Again, this behavior of the MS/MS prefilter is in agreement, but for low masses only, with that anticipated from the Vienna prototype [48].

We further analyze the behavior of the MS/MS prefilter for a m_0 lower than ^{120}Sn set at 63 amu (^{63}Cu) with the adjustable slit fully open, or 50% or 70% closed (S = 100%, 50% and 30%, respectively) and B values set at 10%, 30%, or 50%, while keeping E/B constant. The resulting scans are given in Figure 4. Closing the adjustable slit when B is minimal produces an asymmetrical bandpass window, but with an asymmetry less pronounced than when m_0 was set at 120 amu (Figure 3). When B is minimal (10%) and with a slit 70% closed, or when B is set at 30% with a slit 100% open, it now produces a more symmetric bandpass window,

which was not the case when m_0 was set at 120 amu. Thus, the capability of the MS/MS prefilter to remove low and high masses varies as a function of m_0.

To investigate this issue, we calculated the theoretical total deviation in the X direction (i.e., the direction of the electric field in the Wien filter) of a beam as a function of its mass, for masses above and below m_0 as described in ref. 47 (see details in Supplementary Information). The value of the total deviation at the position of the slit (ΔX_{tot}) was shown to be equal to:

$$\Delta X_{tot} = \left(E - \sqrt{\frac{2E_{kin}}{m}} B \right) \frac{q l^2}{4E_{kin}} + l_2 \frac{\left(\frac{E}{B} - v_{init}\right) sin\left(\frac{\omega l}{v_{init}}\right)}{\frac{E}{B} + \left(v_{init} - \frac{E}{B}\right) cos\left(\frac{\omega l}{v_{init}}\right)}$$

where E_{kin} is the kinetic energy of ions, m their mass, v_{init} the initial velocity, $\omega = qB/m$ and l the length of the Wien filter along its main axis. This non-linear equation giving ΔX_{tot} as a function of the initial velocity was solved numerically to calculate the deviation in the x-direction for a given mass, as a function of slit opening and magnetic field in the first Wien filter. As shown in Figure 5, the calculated deviation of the beam as a function of the magnetic field is not symmetric for high and low masses. For m_0 = 120 amu, the vertical deviation for a B value of 100% will be 3 mm and 4 mm for a variation of mass-to-charge of ± 20%, respectively. Thus, by either increasing the magnetic field (or closing symmetrically the slit) our calculations show an asymmetric trimming of ion in the low mass and high mass regions, with low mass being more efficiently eliminated.

To evaluate the reliability of the modelling, we next compare the theoretical calculations with the results obtained at m_0 set at 120 amu and 63 amu with different combinations of B and S values shown in Figure 3 and Figure 4. The variation of the asymmetry of the bandpass window as a function of B value is given for m_0 set at 120 amu and 63 amu in Figure 6A and figure 6B, respectively, and shows a good agreement between modelled and measured results. The modelled transmitted low and high masses adequately reproduce the observation that the symmetry of the bandpass window is improved for weak magnetic field value (30%) when m_0 is low (Figure 6B). We note, however, a small discrepancy for high masses between 150 and 200 amu that we attribute to an inaccurate measurement of the bandpass window due to a lack of elements with those masses (PGE and REE) in the 33 elements solution. The variation of the asymmetry of the bandpass window as a function of

the slit aperture is given for m_0 set at 120 amu and 63 amu in Figure 7A and figure 7B, respectively. Again, a good agreement is observed between modelled and measured results, which confirms that the adjustable slit needs to be closed to about 70% to produce a more symmetric bandpass.

In conclusion, the double Wien prefiltering is a highly efficient system for the on-line removal of elements that are 30 to 20 amu lower than a given analyte. It provides an ion beam that only contains the elements of interest to enter the CRC to allow better resolved reactions and collisions.

On-line removal of matrix effects

Copper isotopes were measured on the Nu Plasma and Neoma MS/MS according to instrument parameters given in Table 1. For the Neoma MS/MS, setting the axial mass at ^{66}Zn and the magnetic field at 30% with the adjustable slit 70% open efficiently removes any possible argide interferences (Figure S2). When Na is added in the Cu-Zn solution with a Na/Cu ratio of 10, the MS/MS prefiltering efficiently removes Na, which is 43 amu lighter than ^{66}Zn (Figure S3). However, a peak scan in an acid blank solution containing only Na still shows the existence of the $^{40}ArNa^+$ compound that interferes with the $^{63}Cu^+$ isobar (Figure S4), demonstrating that the formation of the $^{40}ArNa^+$ ion mainly occurs in the plasma source. The addition of He in the CRC is necessary to remove this argide (Figure S5), however we found the appearance of a new interference on ^{68}Zn when He is introduced (Figure S6). We hypothesize that the interfering species might be formed of a O- and, in a lesser extent, N-based compound as these are known to form in wet conditions in the presence of He [60].

The instrumental mass fractionation shows a linear relationship between $\ln(^{65}Cu/^{63}Cu)$ vs. $\ln(^{66}Zn/^{64}Zn)$ with a slope of 0.998 ± 0.049 and an intercept of 0.235 ± 0.036 (R^2 = 0.963) and, despite the presence of the double-Wien filter and the use of He in the CRC, the fractionation factors fCu and fZn are calculated to be 2.11 ± 0.01 (± 2 SD, n = 18) and 2.13 ± 0.01 (± 2 SD, n = 18), respectively, thus similar to values reported in the literature (e.g., with the Plasma 54 instrument [2]).

In the present study, we have evaluated the non-spectral matrix effects of Na with a Cu-normalized ratio ranging from 1 to 25 using the Nu Plasma (Figure 8A) and to 50 using the Neoma MS/MS (Figure 8B). The results obtained with the Nu Plasma compare well with the literature values, regardless of the type of MC-ICPMS used, the Sapphire (Nu Instrument,

Wrexham, UK) in the conventional high energy pathway [61] or the Neptune [5,6,10,42]. The overall results show that the δ^{65}Cu value begins to be significantly offset with a Na/Cu ratio of 1 (Figure 8A). In comparison, the measured δ^{65}Cu values with the Neoma MS/MS remain accurate up to a Na/Cu ratio of 10 (Figure 8B, Figure S7). At this stage, the δ^{65}Cu value is no longer corrected and becomes negatively biased, suggesting that the $^{40}Ar^{23}Na^{+}$ interference is no longer spectral and becomes a matrix effect.

Accuracy of the δ^{65}Cu values measurements

Blank signal measured in HNO_3 2% is 12 mV on ^{63}Cu for a sensitivity of about 5 V/ppm (Table 1). The repeatability (or short-term external precision) was evaluated by repeated analyses of the SRM-976 solution at 0.2 mg/L, which yields an initial and preliminary value of 0.03‰ (± 2SD, n = 13), which will need to be confirmed by further analyses.

Eight geological CRM were purified for Cu using a single step preparation ion-exchange chromatography using the PrepFAST-MC system, and the measured δ^{65}Cu values are given in Table S1 and shown in Figure 9. The accuracy with already reported δ^{65}Cu values is in good agreement, e.g., -0.04‰ for BHVO-1, 0.02% for W2a, 0.00‰ for BIR-1, 0.03‰ for AGV-2. We measured, however, a slightly higher δ^{65}Cu value (0.22‰) for BCR-1 than previously measured on different instruments (0.09 ± 0.02‰, Table S1), for which we do not have at the moment any explanation to propose. Three blood samples show similar δ^{65}Cu values on the Nu Plasma and the Neoma MS/MS within 0.05‰ uncertainties.

CONCLUSIONS

Our results indicate that the double-Wien prefiltering system of the Neoma MC-ICPMS/MS produces an asymmetrical mass window transmitted through the slit located between the two filters, relative to the selected axial mass-to-charge value, with removal of low masses being more effective than removal of high masses. This feature is a normal consequence of the ion trajectories in a Wien filter, and taking into account this feature will be necessary during the tuning of the instrument, notably for low masses. Care we be also necessary to avoid trimming the analyte isotope signals, that could possibly produce instrumental instability and isotope fractionation. For well identified reactions and collisions, the possibility of removing part of the mass range will be of significant importance for laser

ablation research, the double-Wien prefiltering will probably allow a neater ion beam to enter the CRC.

CONFLICT OF INTEREST

There are no conflicts to declare.

ACKNOWLEDGEMENTS

The authors are grateful to Ryan Ickert and an anonymous reviewer for constructive comments that improve the quality of the manuscript, and the Institut National des Sciences de l'Univers (INSU) of the CNRS, the LABEX Lyon Institute of Origins (ANR-10-LABX-0066) of the Université de Lyon, the Fonds Recherche of the Ecole Normale Supérieure de Lyon, and the Laboratoire de Géologie de Lyon: Terre, Planètes, Environnements, for their financial support.

6. REFERENCES

1. Shields WR, Murphy TJ, Garner EL. Absolute Isotopic Abundance Ratio and the Atomic Weight of a Reference Sample of Copper. *J Res. Natl. Bur. Stand. A Phys. Chem*. 1964, **68**, 589-592.

2. Maréchal CN, Télouk P, Albarède F. Precise analysis of copper and zinc isotopic compositions by plasma-source mass spectrometry. *Chem. Geol*. 1999, **156**, 251-273.

3. Larner F, Rehkämper M, Coles BJ, et al. A new separation procedure for Cu prior to stable isotope analysis by MC-ICP-MS. *J. Anal. At. Spectrom*. 2011, **26**, 1627-1632.

4. Moeller K, Schoenberg R, Pedersen RB, Weiss D, Dong S. Calibration of the New Certified Reference Materials ERM-AE633 and ERM-AE647 for Copper and IRMM-3702 for Zinc Isotope Amount Ratio Determinations. *Geostand. Geoanalytical Res*. 2012, **36**, 177-199.

5. Hou Q, Zhou L, Gao S, Zhang T, Feng L, Yang L. Use of Ga for mass bias correction for the accurate determination of copper isotope ratio in the NIST SRM 3114 Cu standard and geological samples by MC-ICPMS. *J. Anal. At. Spectrom*. 2015, **31**, 280-287.

6. Lauwens S, Costas-Rodríguez M, Vanhaecke F. Ultra-trace Cu isotope ratio measurements via multi-collector ICP-mass spectrometry using Ga as internal standard: an approach applicable to micro-samples. *Anal. Chim. Acta*. 2018, **1025**, 69-79.

7. Luck JM, Othman DB, Barrat JA, Albarède F. Coupled ^{63}Cu and ^{16}O excesses in chondrites. *Geochim. Cosmochim. Acta*. 2003, **67**, 143-151.

8. Moynier F, Albarède F, Herzog GF. Isotopic composition of zinc, copper, and iron in lunar samples. *Geochim. Cosmochim. Acta*. 2006, **70**, 6103-6117.

9. Liu SA, Huang J, Liu J, et al. Copper isotopic composition of the silicate Earth. *Earth Planet. Sci. Lett*. 2015, **427**, 95-103.

10. Liu SA, Li D, Li S, et al. High-precision copper and iron isotope analysis of igneous rock standards by MC-ICP-MS. *J. Anal. At. Spectrom*. 2013, **29**, 122-133.

11. Asael D, Matthews A, Oszczepalski S, Bar-Matthews M, Halicz L. Fluid speciation controls of low temperature copper isotope fractionation applied to the Kupferschiefer and Timna ore deposits. *Chem. Geol*. 2009, **262**, 147-158.

12. Smuda J, Dold B, Spangenberg JE, Pfeifer HR. Geochemistry and stable isotope composition of fresh alkaline porphyry copper tailings: Implications on sources and mobility of elements during transport and early stages of deposition. *Chem. Geol*. 2008, **256**, 62-76.

13. Asael D, Matthews A, Bar-Matthews M, Halicz L. Copper isotope fractionation in sedimentary copper mineralization (Timna Valley, Israel). *Chem. Geol*. 2007, **243**, 238-254.

14. Little SH, Vance D, McManus J, Severmann S, Lyons TW. Copper isotope signatures in modern marine sediments. *Geochim. Cosmochim. Acta*. 2017, **212**, 253-273.

15. Wang Q, Zhou L, Little SH, Liu J, Feng L, Tong S. The geochemical behavior of Cu and its isotopes in the Yangtze River. *Sci. Total Environ*. 2020, **728**, 138428.

16. Vance D, Archer C, Bermin J, et al. The copper isotope geochemistry of rivers and the oceans. *Earth Planet. Sci. Lett*. 2008, **274**, 204-213.

17. Bermin J, Vance D, Archer C, Statham PJ. The determination of the isotopic composition of Cu and Zn in seawater. *Chem. Geol*. 2006, **226**, 280-297.

18. Takano S, Tanimizu M, Hirata T, Sohrin Y. Isotopic constraints on biogeochemical cycling of copper in the ocean. *Nat. Commun*. 2014, **5**, 5663.

19. Souto-Oliveira CE, Babinski M, Araújo DF, Weiss DJ, Ruiz IR. Multi-isotope approach of Pb, Cu and Zn in urban aerosols and anthropogenic sources improves tracing of the atmospheric pollutant sources in megacities. *Atmospheric Environment*. 2019, **198**, 427-437.

20. Gonzalez RO, Strekopytov S, Amato F, Querol X, Reche C, Weiss D. New Insights from Zinc and Copper Isotopic Compositions into the Sources of Atmospheric Particulate Matter from Two Major European Cities. *Environ. Sci. Technol*. 2016, **50**, 9816-9824.

21. Dong S, Ochoa Gonzalez R, Harrison RM, et al. Isotopic signatures suggest important contributions from recycled gasoline, road dust and non-exhaust traffic sources for copper, zinc and lead in PM10 in London, United Kingdom. *Atmos. Environ*. 2017, **165**, 88-98.

22. Fekiacova Z, Cornu S, Pichat S. Tracing contamination sources in soils with Cu and Zn isotopic ratios. *Sci. Total Environ*. 2015, **517**, 96-105.

23. El Azzi D, Viers J, Guiresse M, et al. Origin and fate of copper in a small Mediterranean vineyard catchment: New insights from combined chemical extraction and δ65Cu isotopic composition. *Sci. Total Environ*. 2013, **463**, 91-101.

24. Kříbek B, Šípková A, Ettler V, et al. Variability of the copper isotopic composition in soil and grass affected by mining and smelting in Tsumeb, Namibia. *Chem. Geol*. 2018, **493**, 121-135.

25. Costas-Rodríguez M, Anoshkina Y, Lauwens S, Van Vlierberghe H, Delanghe J, Vanhaecke F. Isotopic analysis of Cu in blood serum by multi-collector ICP-mass spectrometry: a new approach for the diagnosis and prognosis of liver cirrhosis? *Metallomics*. 2015, **7**, 491-498.

26. Hastuti AAMB, Costas-Rodríguez M, Anoshkina Y, Parnall T, Madura JA, Vanhaecke F. High-precision isotopic analysis of serum and whole blood Cu, Fe and Zn to assess possible homeostasis alterations due to bariatric surgery. *Anal. Bioanal. Chem*. 2020, **412**, 727-738.

27. Lamboux A, Couchonnal-Bedoya E, Guillaud O, et al. The blood copper isotopic composition is a prognostic indicator of the hepatic injury in Wilson disease†. *Metallomics*. 2020, **12**, 1781-1790.

28. Moynier F, Creech J, Dallas J, Le Borgne M. Serum and brain natural copper stable isotopes in a mouse model of Alzheimer's disease. *Sci. Rep*. 2019, **9**, 11894.

29. Solovyev N, El-Khatib AH, Costas-Rodríguez M, et al. Cu, Fe, and Zn isotope ratios in murine Alzheimer's disease models suggest specific signatures of amyloidogenesis and tauopathy. *J. Biol. Chem.* 2021, **296**, 100292.

30. Sauzéat L, Bernard E, Perret-Liaudet A, et al. Isotopic Evidence for Disrupted Copper Metabolism in Amyotrophic Lateral Sclerosis. *iScience*. 2018, **6**, 264-271.

31. Balter V, Nogueira da Costa A, Bondanese VP, et al. Natural variations of copper and sulfur stable isotopes in blood of hepatocellular carcinoma patients. *Proc. Natl. Acad. Sci. USA*. 2015, **112**, 982-985.

32. Télouk P, Puisieux A, Fujii T, et al. Copper isotope effect in serum of cancer patients. A pilot study. *Metallomics*. 2015, **7**, 299-308.

33. Wang W, Liu X, Zhang C, et al. Identification of two-dimensional copper signatures in human blood for bladder cancer with machine learning. *Chem. Sci*. 2022, **13**, 1648-1656.

34. Jaouen K, Balter V, Herrscher E, Lamboux A, Telouk P, Albarède F. Fe and Cu stable isotopes in archeological human bones and their relationship to sex. *Am. J. Phys. Anthropol*. 2012, **148**, 334-340.

35. Jaouen K, Herrscher E, Balter V. Copper and zinc isotope ratios in human bone and enamel. *Am. J. Phys. Anthropol*. 2017, **162**, 491-500.

36. Boucher RD, Alavi SE, de Jong HN, Godfrey LV, Vogel ER. Stable isotope evidence (Fe, Cu) suggests that sex, but not aging is recorded in rhesus macaque (Macaca mulatta) bone. *Am. J. Phys. Anthropol.*. 2021, **176**, 80-92.

37. Aragón E, Montero-Ruiz I, Polzer ME, van Duivenvoorde W. Shipping metal: Characterisation and provenance study of the copper ingots from the Rochelongue underwater site (Seventh–Sixth century BC), West Languedoc, France. *J. Archaeol. Sci.: Reports*. 2022, **41**, 103286.

38. Desaulty AM, Telouk P, Albalat E, Albarède F. Isotopic Ag–Cu–Pb record of silver circulation through 16th–18th century Spain. *Proc. Natl. Acad. Sci*. USA 2011, **108**, 9002-9007.

39. Mathur R, Titley S, Hart G, Wilson M, Davignon M, Zlatos C. The history of the United States cent revealed through copper isotope fractionation. *J. Archaeol. Sci*. 2009, **36**, 430-433.

40. Kidder JA, Voinot A, Sullivan KV, et al. Improved ion-exchange column chromatography for Cu purification from high-Na matrices and isotopic analysis by MC-ICPMS. *J. Anal. At. Spectrom*. 2020, **35**, 776-783.

41. Maréchal C, Albarède F. Ion-exchange fractionation of copper and zinc isotopes. *Geochim. Cosmochim. Acta*. 2002, **66**, 1499-1509.

42. Wang Q, Zhou L, Feng L, et al. Use of a Cu-selective resin for Cu preconcentration from seawater prior to its isotopic analysis by MC-ICP-MS. *J. Anal. At. Spectrom*. 2020, **35**, 2732-2739.

43. Schwieters J, Elliott TR, Coath CD. US 10867780B2 Multi detector mass spectrometer and spectrometry method filter, 2020.

44. Pfeifer M, Lewis J, Coath C, Schwieters J, Elliott T. In situ titanium isotope measurements in meteorites using the collision cell MC-ICPMS, Proteus. Goldschmidt Abstracts. 2019.

45. Bevan D, Coath C, Lewis J, Schwieters J, Lloyd N, Craig G, et al. Detrital K-feldspar. geochronology by collision cell MC-ICPMS/MS. Goldschmidt Abstracts. 2020.

46. Bevan D, Coath CD, Lewis J, et al. In situ Rb–Sr dating by collision cell, multicollection inductively-coupled plasma mass-spectrometry with pre-cell mass-filter, (CC-MC-ICPMS/MS). *J. Anal. At. Spectrom*. 2021, **36**, 917-931

47. Schwieters J, Jung G. WO 2019/180045 A1. Mass spectrometer, 2019.

48. Craig G, Wehrs H, Bevan DG, et al. Project Vienna: A Novel Precell Mass Filter for Collision/Reaction Cell MC-ICPMS/MS. *Anal Chem*. 2021, **93**, 10519-10527.

49. Dauphas N, Hopp T, Craig G, et al. In situ ^{87}Rb–^{87}Sr analyses of terrestrial and extraterrestrial samples by LA-MC-ICP-MS/MS with double Wien filter and collision cell technologies. *J. Anal. At. Spectrom*. 2022, **37**, 2420-2441.

50. Télouk P, Albalat E, Tacail T, Arnaud-Godet F, Balter V. Steady analyses of potassium stable isotopes using a Thermo Scientific Neoma MC-ICP-MS. *J. Anal. At. Spectrom*. 2022, **37**, 1259-1264.

51. F.J. Flanagan Descriptions and Analyses of Eight New USGS Rock Standards. U.S.G.S. Bull. **840**, 1976.

52. Flanagan FJ. U.S. Geological Survey silicate rock standards. *Geochim. Cosmochim. Acta*. 1967, **31**, 289-308.

53. Flanagan FJ. *Three USGS Mafic Rock References Samples, W-2, DNC-1, and BIR-1*. U.S.G.S. Bull. **1624**, 1984.

54. Imai N, Terashima S, Itoh S, Ando A. Compilation of Analytical Data for Minor and Trace Elements in Seventeen Gsj Geochemical Reference Samples, "Igneous Rock Series." *Geostand. Newsl*. 1995, **19**, 135-213.

55. Enge TG, Field MP, Jolley DF, Ecroyd H, Kim MH, Dosseto A. An automated chromatography procedure optimized for analysis of stable Cu isotopes from biological materials. *J. Anal. At. Spectrom*. 2016, **31**, 2023-2030.

56. Plies E, Marianowski K, Ohnweiler T. The Wien filter: History, fundamentals and modern applications. *Nucl. Instrum. Methods Phys. Res. A*. 2011, **645**, 7-11.

57. Curtis GH, Silcox J. A Wien filter for use as an energy analyzer with an electron microscope. *Rev. Sci. Instrum*. 1971, **42**, 630-637.

58. McCurdy E, Woods G. The application of collision/reaction cell inductively coupled plasma mass spectrometry to multi-element analysis in variable sample matrices, using He as a non-reactive cell gas. *J. Anal. At. Spectrom*. 2004, **19**, 607-615.

59. R: The R Project for Statistical Computing. 2023.

60. A. Dexter, K. Appelblad, P. Ingle, H. Batey, J. Reid, L. Sharp. The effect of adventitious water in hexapole collision cell inductively coupled plasma mass spectrometry. *J. Anal. At. Spectrom*. 2002, **17**, 183-188.

61. J. Wang, B.X. Su, D.M. Tang, et al. High-precision copper isotopic analysis using a Nu Sapphire MC-ICP-MS. *J. Anal. At. Spectrom*. 2022, **37**, 2589-2598.

Figure captions

Fig. 1: Schematic overview of the ion path in the Neoma prefiltering MS/MS system. 1, entrance aperture; 2, first lens (L1) to focus; 3, first Wien filter; 4, baffles; 5, adjustable slit; 6 second lens (L2) to inverse; 7, second Wien filter; 8, third lens (L3) to focus; 9, exit aperture; 10, fourth lens (L4) to focus; 11, collision/reaction cell.

Fig. 2: **A**, Overall signal intensities for a mass scan with m_0 = 120 from 20 to 250 m/z with induction set at B = 10%. **B**, Difference of signal intensities between two successive mass scans with induction set at B(n+10) and B(n), with n increasing by a 10% increment. Amplifier of the axial collector was set at 10^{11} Ω.

Fig. 3: Overall signal intensities for a mass scan with m_0 = 120 from 20 to 250 m/z for various values of induction and adjustable slit aperture. Amplifier of the axial collector was set at 10^{11} Ω.

Fig. 4: Overall signal intensities for a mass scan with m_0 = 63 from 20 to 250 m/z for various values of induction and adjustable slit aperture. Amplifier of the axial collector was set at 10^{11} Ω.

Fig. 5: Deviation in x-axis at the position of the slit located between the two Wien filters for various masses shifted by X% as labeled on the curves, as a function of magnetic field in the first Wien filter given in %. The line with no deviation corresponds to the mass m_0 = 120 amu. The length of the Wien is assumed to be 7 cm and the kinetic energy of the singly charged ions is 2 keV. Details for calculations are given in the Supplementary Information.

Fig. 6: Calculated low mass (dotted line) and high mass (dashed line) transmitted through the slit located between the two Wien filters as a function of the magnetic field in the first Wien filter (in %). Details for calculations are given in the Supplementary Information. **A**, m_0=120 amu. Solid circles are from direct measurements as shown in Figure 3 with a threshold value of 1V. **B**, m_0=63 amu. Solid circles are from direct measurements as shown in Figure 4 with a threshold value of 1V.

Fig. 7: Calculated low mass (dotted line) and high mass (dashed line) transmitted through the slit located between the two Wien filters as a function of the opening of the slit (in %). Details for calculations are given in the Supplementary Information. **A**, m_0=120 amu. Solid circles are from direct measurements as shown in Figure 3 with a threshold value of 1V. **B**, m_0=63 amu. Solid circles are from direct measurements as shown in Figure 4 with a threshold value of 1V.

Fig. 8: **A**, Matrix effects on the δ^{65}Cu value of the SRM-976 solution as a function of the Na/Cu ratio measured with the Nu Plasma and compared to the literature. The light grey area represents ± 0.05‰ deviation. The error bars are ± 2SD of the mean. **B**, Matrix effects on the δ^{65}Cu value of the SRM-976 solution as a function of the Na/Cu ratio measured with the Neoma MS/MS. Several He flow are tested. The light grey area represents ±0.05‰ deviation and the dark grey area represents the hull of the panel A for comparison.

Fig. 9: δ^{65}Cu values measured in the present study (purple) and compared with the literature (black). The error bars are ± 2SD of the mean (the number of replicates is given in Table S1).

Supplementary information for:

Performance of the double-Wien filter of the Neoma MC-ICPMS/MS with an application to copper stable isotope compositions

Philippe Télouk, Emmanuelle Albalat, Bernard Bourdon, Francis Albarède, Vincent Balter

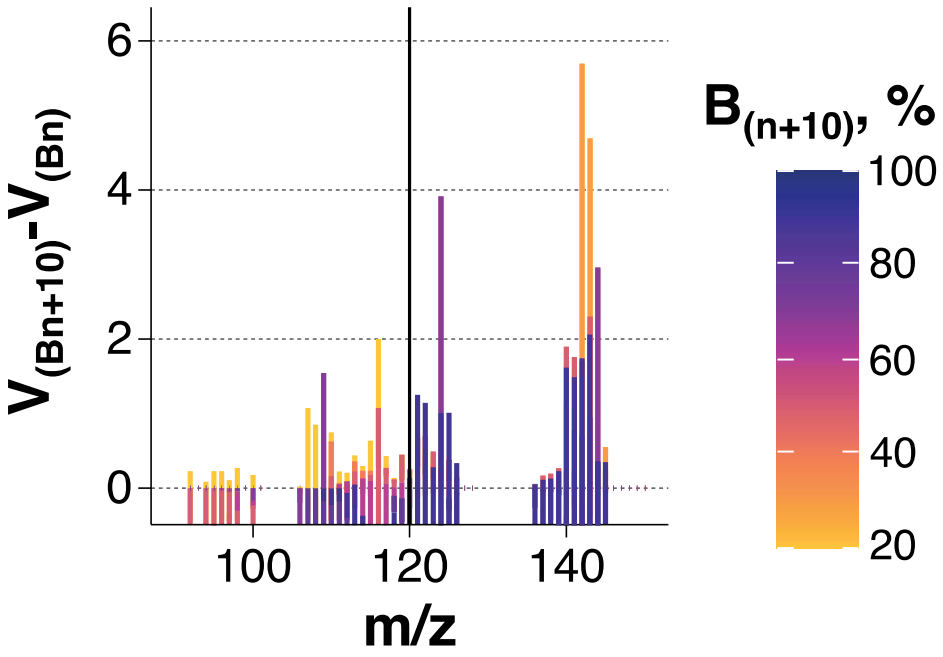

Fig. S1: Difference of overall transmissions from 90 to 150 m/z between two successive masses scans with induction set at B(n+10) and B(n), with n increasing by 10% increment.

Ion trajectories in a Wien filter as a function of mass/charge ratio

We assume that the electric and magnetic field are homogeneous and have orthogonal components in the y and x direction, respectively. The z direction corresponds to the main axis of ion trajectories as shown in Figure S1. The ions are injected into the Wien filter with an energy E_{kin}. The electric and magnetic forces exerted on an ion of charge q and mass m can be written as:

$$q\vec{E} + q\vec{v} \times \vec{B} = m\frac{d\vec{v}}{dt} \qquad (1)$$

The electrical field vector has the following components (E, 0, 0) while the magnetic field has the component (0, B, 0). If one uses cartesian coordinates as defined in figure S1, equation () is equivalent to the following equation for each coordinate x,y and z:

$$m\frac{dv_x}{dt} = qE - qv_zB \qquad (2)$$
$$m\frac{dv_y}{dt} = 0 \qquad (3)$$
$$m\frac{dv_z}{dt} = qv_xB \qquad (4)$$

We assume that the initial velocity in the direction v_y is equal to zero and that at t=0, y=0, thus the second equation is easily integrated to give:

$$y = y_0$$

We thus obtain a system of two coupled second-order equations in the x and z direction:

$$m\dot{v_x} = qE - qv_zB \quad (5)$$
$$\dot{v_z} = \frac{qB}{m}v_x \qquad (6)$$

We differentiate equation (6) with respect to time and replace it in equation (5):

$$\dot{v_x} = \frac{m}{qB}\ddot{v_z} \qquad (7)$$
$$\frac{m}{qB}\ddot{v_z} = \frac{qE}{m} - \frac{qB}{m}v_z \quad (8)$$

This equation can be rearranged to give:

$$\ddot{v_z} + \left(\frac{qB}{m}\right)^2 v_z = \left(\frac{q}{m}\right)^2 EB \quad (9)$$

It is known from textbooks that the solutions of such equations can first be found by solving the homogeneous equation:

$$\ddot{v_z} + \left(\frac{qB}{m}\right)^2 v_z = 0 \quad (10)$$

A solution to this equation is written as:

$$v_z = Acos(\omega t) + Bsin(\omega t) \qquad (11)$$

With the frequency ω equal to:

$$\omega = \frac{qB}{m} \qquad (12)$$

We now look for a particular solution to the complete equation. A possible solution could be $v_z = constant\ k$. In this case:

$$\dot{v_x} = 0 \qquad (13)$$

The solution can be written:

$$\left(\frac{qB}{m}\right)^2 k = \left(\frac{q}{m}\right)^2 EB \qquad (14)$$

Hence :

$$k = \frac{E}{B} \qquad (15)$$

The solution of the complete equation is the sum of the solution of the homogenous equation and the particular solution:

$$v_z = Acos(\omega t) + Bsin(\omega t) + \frac{E}{B} \qquad (16)$$

We now apply the initial condition that $v_z = v_{init}$ at t=0. In our system, all the ions are accelerated by a potential of approximately 2 kV to a constant kinetic energy.

$$v_{init} = A + \frac{E}{B} \qquad (17)$$

Or :

$$A = v_{init} - \frac{E}{B} \qquad (18)$$

In order to determine the value of B, we apply the initial condition for v_x :

$$\dot{v_z} = -A\omega sin(\omega t) + B\omega cos(\omega t) \qquad (19)$$

Thus, based on equation (7), we can write:

$$v_x = \frac{m\omega}{qB}[-Asin(\omega t) + Ccos(\omega t)] \qquad (20)$$

The initial condition is that $v_x = 0$ at t=0, hence:

$$\frac{m\omega}{qB}C = 0 \qquad (21)$$

Thus, we find :

$$C = 0$$

$$v_z = \left(v_{init} - \frac{E}{B}\right)cos(\omega t) + \frac{E}{B} \qquad (22)$$

By integrating with respect to t, we find the value of z(t):

$$z(t) = \frac{1}{\omega}\left(v_{init} - \frac{E}{B}\right)sin(\omega t) + \frac{E}{B}t + D \qquad (23)$$

The constant D is equal to zero because z(t)=0 at t=0. The value of v_x and x(t) can also be deduced from this:

$$v_x = \frac{m\omega}{qB}\left[-\left(v_{init} - \frac{E}{B}\right)sin(\omega t)\right] = -\left(v_{init} - \frac{E}{B}\right)sin(\omega t) \qquad (24)$$

By integrating this equation, we can derive the value of x(t):

$$x(t) = \frac{1}{\omega}\left(v_{init} - \frac{E}{B}\right)cos(\omega t) + K \qquad (25)$$

We now apply the initial condition x(t)=0 at t=0:

$$\frac{1}{\omega}\left(v_{init} - \frac{E}{B}\right) + K = 0 \qquad (26)$$

Or :

$$K = -\frac{1}{\omega}\left(v_{init} - \frac{E}{B}\right) \qquad (27)$$

The solution for x(t) is thus:

$$x(t) = \frac{1}{\omega}\left(v_{init} - \frac{E}{B}\right)(cos(\omega t) - 1) \qquad (28)$$

We then use a Taylor expansion of $cos(\omega t)$ assuming that ωt is small:

$$cos(\omega t) \approx 1 - \frac{(\omega t)^2}{2} \qquad (29)$$

$$x(t) = \frac{1}{\omega}\left(\frac{E}{B} - v_{init}\right)\frac{(\omega t)^2}{2} \qquad (30)$$

We also make a Taylor expansion of $cos(\omega t)$ in the equation giving z(t):

$$sin(\omega t) \approx \omega t - \frac{\omega t^3}{6}$$

If we choose z(t) such that it is equal to l:

$$z(t) = l = \frac{1}{\omega}\left(v_{init} - \frac{E}{B}\right)\omega t + \frac{E}{B}t = v_{init}t$$

We now wish to express x(t) at the time when the ions exit the Wien filter. To do so, one can use the ions that have an initial velocity equal to $v_0 = E/B$. In this case, their velocity v_x is equal to zero, according to equation () and x(t) is also equal to zero for these ions. The time t can be expressed as:

$$t = \frac{l}{v_{init}} \qquad (31)$$

This equation can be inserted into equation (30):

$$x(t) = \frac{1}{\omega}\left(\frac{E}{B} - v_{init}\right)\frac{(\omega l/v_{init})^2}{2} \qquad (32)$$

$$x(t) = \frac{m}{qB}\left(\frac{E}{B} - v_{init}\right)\left(\frac{qB}{m}\right)^2\frac{(l/v_{init})^2}{2} = \left(\frac{E}{B} - v_{init}\right)\frac{qB}{m}\frac{(l/v_{init})^2}{2} \qquad (33)$$

$$x(t) = (E - v_{init}B)\frac{ql^2}{2mv_{init}^2} \qquad (34)$$

The value v_{init} can be expressed as a function of the initial kinetic energy of the ions E_{kin} :

$$v_{init} = \sqrt{\frac{2E_{kin}}{m}} \qquad (35)$$

This expression is inserted into equation (34):

$$x(z = l) = \left(E - \sqrt{\frac{2E_{kin}}{m}}B\right)\frac{ql^2}{2m_0v_0^2} \qquad (36)$$

We finally obtained the following equation for the deviation in the x direction of a beam with ions of mass m:

$$x(z = l) \sim \left(E - \sqrt{\frac{2E_{kin}}{m}}B\right)\frac{ql^2}{4E_{kin}} \qquad (37)$$

A more rigorous solution can be obtained by solving for the value of t the non-linear equation:

$$z(t) = \frac{1}{\omega}\left(v_{init} - \frac{E}{B}\right) sin(\omega t) + \frac{E}{B} t = l \quad (38)$$

Once the value of t is obtained, one can calculate the corresponding value of x(t). We have checked numerically using a Matlab code that the results are almost identical to those given with the approximate equation (37).

One should point out, however that the deviation calculated with equation (37) does not correspond to the vertical divergence of the beam at the position of the slit. This slit is located a few cm away from the exit of the Wien filter. This means that one also needs to consider the vertical expansion of the beam in the region where no electrostatic or magnetic force is exerted on the ions. In this case, the equations of the trajectory in x and z become:

$$m\frac{dv_x}{dt} = 0 \quad (39)$$

$$m\frac{dv_y}{dt} = 0 \quad (40)$$

$$m\frac{dv_z}{dt} = 0 \quad (41)$$

The velocities v_x and v_z are constant and the equations can be integrated to yield:

$$x = v_x^0 t + x_0 \quad (42)$$

$$z = v_z^0 t + z_0 \quad (43)$$

We are interested in calculating x for a given value of $z=l_2$ representing the distance between the end of the Wien filter and the defining slit. For the sake of simplicity, we take x_0 and z_0 equal to 0. This yields finally:

$$x = \frac{v_x^0}{v_z^0} l_2 \quad (44)$$

This represent a deviation Δx that can be calculated as a function of l_2 and the velocities in x and z directions at the exit of the Wien filter:

$$\Delta x = l_2 \frac{\left(\frac{E}{B} - v_{init}\right) sin\left(\frac{\omega l}{v_{init}}\right)}{\frac{E}{B} + \left(v_{init} - \frac{E}{B}\right) cos\left(\frac{\omega l}{v_{init}}\right)} \quad (45)$$

This equation must be solved numerically by assuming a value for Δx and one can then obtain the value of v_{init} corresponding to this vertical deviation. This initial velocity is then converted to the mass of the ion using:

$$m = \frac{2E_{kin}}{v_{init}} \quad (46)$$

The total deviation in the x direction is obtained by summing Δx in equation (45) and equation (37):

$$\Delta x_{tot} = \left(E - \sqrt{\frac{2E_{kin}}{m}} B \right) \frac{q l^2}{4E_{kin}} + l_2 \frac{\left(\frac{E}{B} - v_{init}\right) sin\left(\frac{\omega l}{v_{init}}\right)}{\frac{E}{B} + \left(v_{init} - \frac{E}{B}\right) cos\left(\frac{\omega l}{v_{init}}\right)} \qquad (47)$$

These equations were then used to construct the diagram of Figures 5, 6, and 7 based on a Matlab script for different values of magnetic field B and slit opening S given in percent of the total.

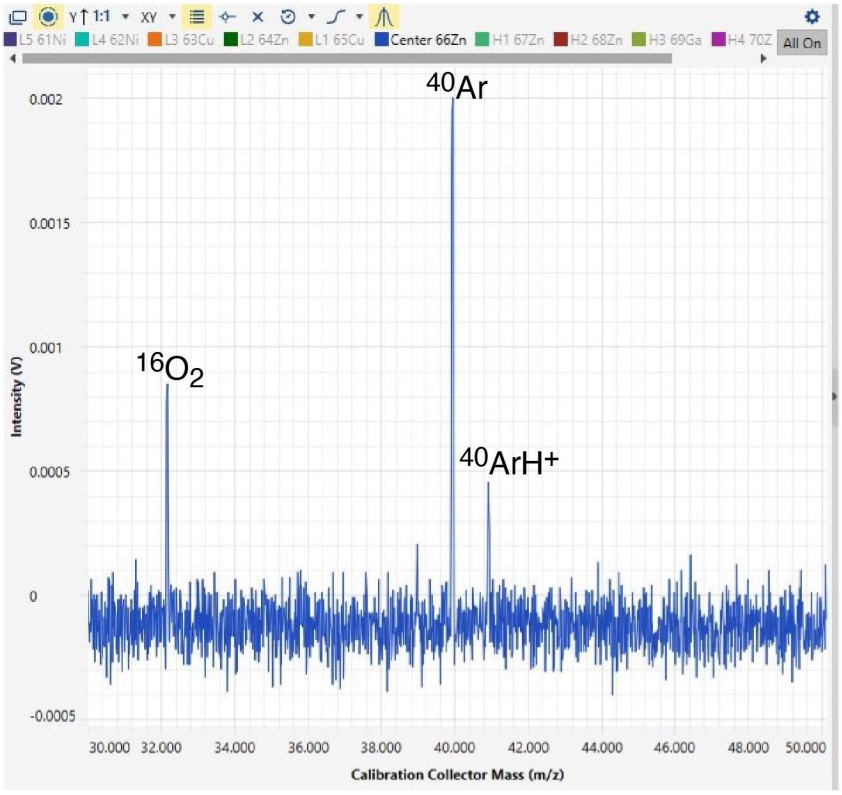

Fig. S2: Masses scan from 30 to 50 m/z with the axial mass set at ^{66}Zn and B = 30%, E = 150 V, S = 70%.

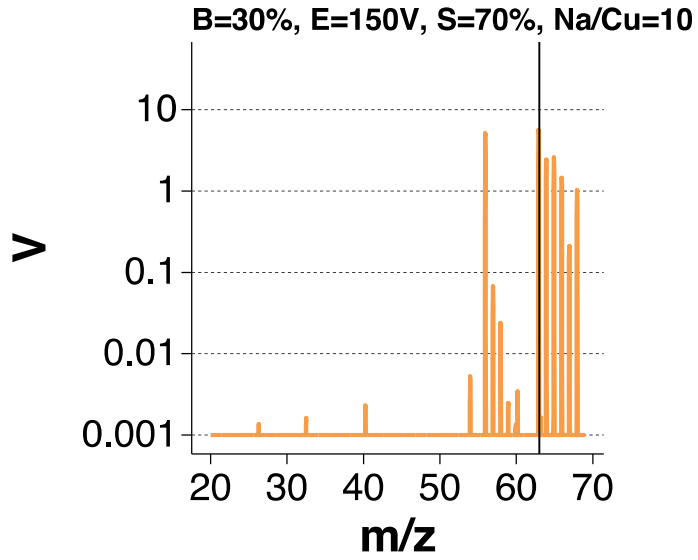

Fig. S3: Overall signal intensities for a mass scan from 20 to 70 m/z of a Cu-Zn-Na solution with Cu and Zn at 200 ng/ml and Na at 2 μg/ml.

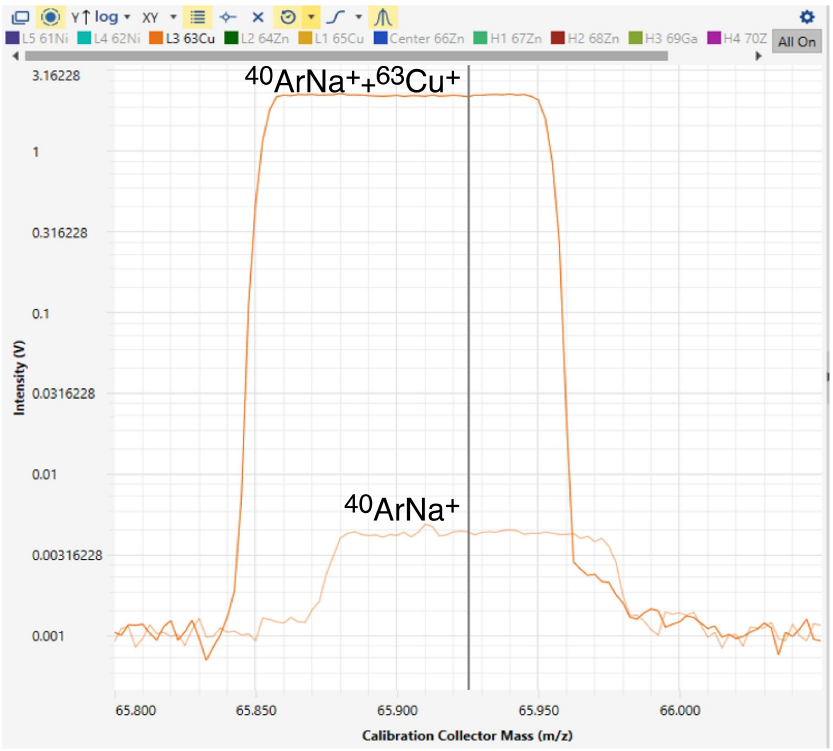

Fig. S4: Peak shapes with the axial mass set at ^{66}Zn and B = 30%, E = 150 V, S = 70% of a HNO_3 0.05M + Na 2 ppm solution (light orange) and of Cu-Zn 200 ppb + Na 2 ppm solution (dark orange), showing the $^{40}ArNa^+$ isobaric interference on $^{63}Cu^+$.

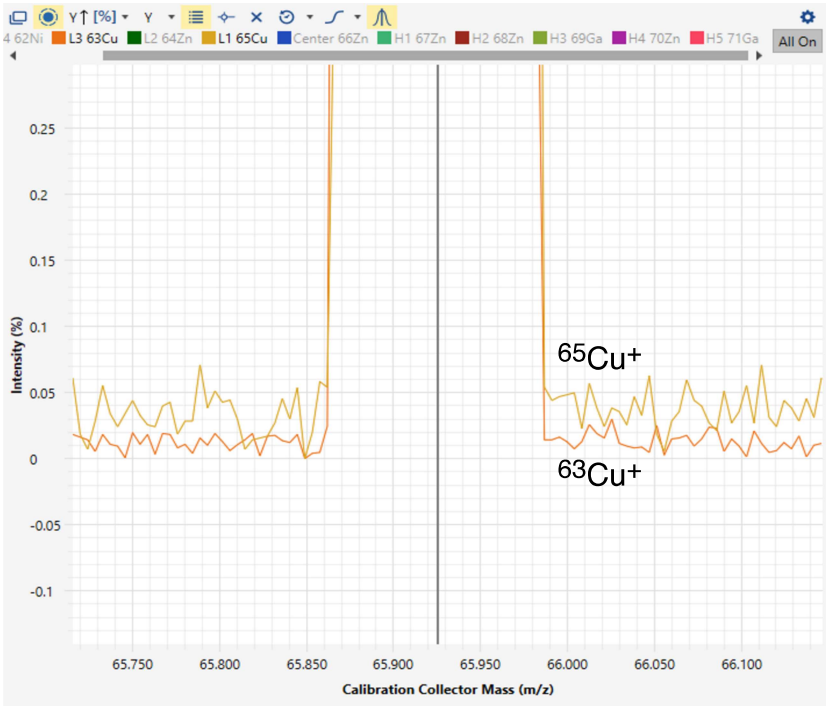

Fig. S5: Peak shapes with the axial mass set at ^{66}Zn and B = 30%, E = 150 V, S = 70% of a Cu-Zn 200 ppb + Na 2 ppm solution with He as a collision gas set at 5 ml/min showing the complete removal of the $^{40}ArNa^{+}$ isobaric interference on $^{63}Cu^{+}$ (dark orange).

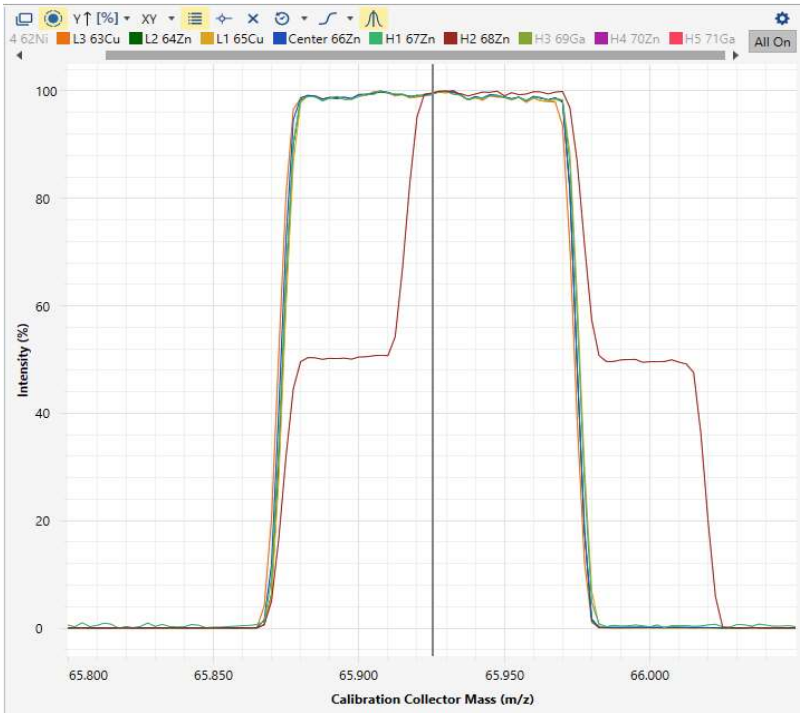

Fig. S6: Peak shapes with the axial mass set at ^{66}Zn and B = 30%, E = 150 V, S = 70% of a Cu-Zn 200 ppb + Na 2 ppm solution with He as a collision gas set at 5 ml/min showing the isobaric interference on $^{68}Zn^{+}$ (brown).

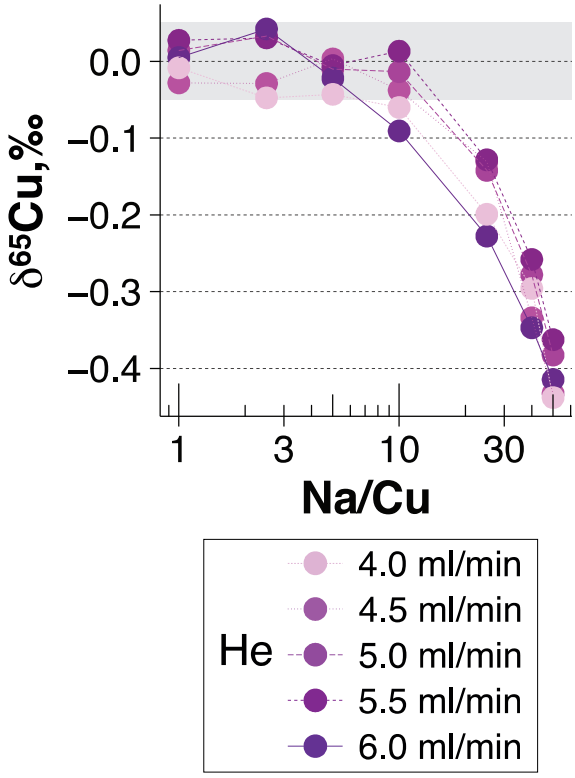

Fig. S7: Matrix effects on the δ^{65}Cu value of the SRM-976 solution as a function of the Na/Cu ratio measured with the Neoma MS/MS. Several He flow are tested. The light grey area represents ±0.05‰ deviation.

Table S1: Copper isotope compositions. § stands for Neoma MS/MS measurements and # stands for Nu Plasma measurements.

	δ^{65}Cu, ‰	± 2 SD, ‰	n	Reference/Status
Standard				
BHVO-1	-0.05		1	This study
	-0.01	0.08	9	Sullivan et al., 2020
JB1 a	0.06		1	This study
DNC 1	0.12		1	This study
W2a	0.11		1	This study
	0.04	0.09	11	Sullivan et al., 2020
	0.10	0.08	4	Liu et al., 2014
	0.11	0.05	4	Liu et al., 2014
	0.11	0.04	4	Liu et al., 2014
BIR-1	0.01		1	This study
	-0.01	0.08	9	Sullivan et al., 2020
	-0.02	0.10	31	Li et al., 2009
	0.08	0.07	6	Moeller et al., 2012
	0.00	0.03	2	Sossi et al., 2015
	0.09	0.08	2	Jeong et al., 2021
	-0.02	0.05	4	Liu et al., 2014
	-0.01	0.04	6	Liu et al., 2014
	-0.03	0.04	4	Liu et al., 2014
	0.01	0.05	4	Liu et al., 2014
	0.02	0.04	4	Liu et al., 2014
	0.02	0.04	3	Liu et al., 2015
AGV-2	0.09		1	This study
	0.09	0.02	2	Jeong et al., 2021
	0.06	0.04	4	Liu et al., 2014
	0.05		1	Liu et al., 2014
	0.06		1	Liu et al., 2015
	0.10		1	Weinstein et al., 2011
	-0.02	0.06	2	Souto-Oliveira et al., 2019
	0.10	0.11	8	Moeller et al., 2012
RGM-1	-0.01		1	This study
BCR-1	0.22		1	This study
	0.07	0.08	6	Archer and Vance, 2004
	0.11	0.12	2	Souto-Oliveira et al., 2019
Sample				
A2 - 33	-0.71§		1	Positive
	-0.65#		1	
A3 - 61	-0.19§		1	Negative
	-0.25#		1	
A5 - 56	-0.09§		1	Negative
	-0.15#		1	